JOURNAL OF AIRCRAFT
Vol. 41, No. 3, May–June 2004

Navier–Stokes Analysis of Tunnel-Wall Interference Effects on Pitching Delta Wings

Yung-Gyo Lee* and C. Edward Lan†
University of Kansas, Lawrence, Kansas 66045

A numerical method for the analysis of tunnel-wall interference effects in forced-oscillation testing is presented. The method is based on the wall-pressure signature concept and utilizes the computed wall-pressure distributions. The induced wall pressure field is computed by using an unsteady three-dimensional full Navier–Stokes solver for a 70-deg pitching delta wing in a wind tunnel. To validate the code, the computed static results are shown to have good agreement with the experimental data of Wentz in lift and drag coefficients. On the other hand, the computed static and dynamic normal force coefficients are, in general, higher than those in a second set of data. However, the predicted hysteresis curves of normal force coefficient in large-amplitude-oscillation testing agree reasonably well with this second set of data. The computed unsteady pressures on the tunnel walls and floor are used to generate the interference flowfield that is analyzed for the upwash and blockage corrections. The corrected results are shown to agree well, in the slope and magnitude of hysteresis loops, with the computed results in free-air conditions. It is also shown that the hysteresis in upwash and blockage corrections increases with the reduced frequency.

Nomenclature

A	=	inviscid flux Jacobian, $\partial E/\partial Q$
a	=	speed of sound
B	=	inviscid flux Jacobian, $\partial F/\partial Q$
C	=	inviscid flux Jacobian, $\partial G/\partial Q$
C_L, C_D, C_m	=	lift, drag, and pitching moment coefficients, respectively
C_{MAC}	=	mean aerodynamic chord
C_N	=	normal force coefficient
C_p	=	pressure coefficient
C_r	=	root chord
$\boldsymbol{E}, \boldsymbol{F}, \boldsymbol{G}$	=	inviscid flux vectors defined in Eqs. (2) and (3)
$\boldsymbol{E}_v, \boldsymbol{F}_v, \boldsymbol{G}_v$	=	viscous flux vectors defined in Eqs. (2) and (3)
h	=	time-step size
J	=	Jacobian of transformation, $\partial(\xi, \eta, \zeta)/\partial(x, y, z)$
k	=	reduced frequency $(= \omega C_{\text{MAC}}/2U_\infty)$
L	=	viscous flux Jacobian, $\partial E_v/\partial Q$
M	=	viscous flux Jacobian, $\partial F_v/\partial Q$
N	=	viscous flux Jacobian, $\partial G_v/\partial Q$
$\boldsymbol{Q}$	=	flux vector defined in Eq. (2)
q	=	dynamic pressure
t	=	physical time
U	=	contravariant velocity in the ξ direction, $\xi_t + \xi_x u + \xi_y v + \xi_z w$
U_∞	=	freestream velocity
u, v, w	=	velocity components along the Cartesian coordinates x, y, and z
V	=	contravariant velocity in the η direction, $\eta_t + \eta_x u + \eta_y v + \eta_z w$
W	=	contravariant velocity in the ζ direction, $\zeta_t + \zeta_x u + \zeta_y v + \zeta_z w$
x, y, z	=	Cartesian coordinates with the positive x axis in the downstream direction and positive y axis in the spanwise direction
ξ, η, ζ	=	body-conforming curvilinear coordinates; ξ represents the streamwise coordinate, η the circumferential coordinate, and ζ the normal coordinate to the body surface
τ	=	pseudotime for subiteration
ω	=	oscillating frequency, rad/s

Subscripts

c	=	corrected
t	=	differentiation with time (t)
τ	=	differentiation with pseudotime (τ)
∞	=	freestream

Superscript

n	=	current time level

Introduction

IT is well known that the static flow phenomena around a delta wing at high angles of attack involve vortex flow generated at the sharp leading edges, vortex bursting, interference from the low-energy wakes, and so forth. These phenomena lead to nonlinear lift variation with the angle of attack. However, when a dynamic motion is involved, for example, a pitching delta wing at a certain reduced frequency, the unsteady effects, as exhibited in aerodynamic hysteresis, would be present because of the lag in flow separation and reattachment and/or vortex bursting. The extent of these changes depends on parameters such as the pitch rate, pitching amplitude, motion history, freestream Mach number, and so on. Numerous subsonic experimental studies have been made to investigate the flow structures over steady and oscillating delta wings. In particular, Wentz and Kohlman[1] conducted a comprehensive static experimental research on delta wings with various apex angles. More recent research has focused on oscillating delta wings. Flow visualization has shown the presence of hysteresis in the measured vortex burst locations. Wolffelt,[2] Soltani et al.,[3] and Torlund[4] have all reported force and moment data on oscillating delta wings.

Many numerical investigations were also conducted to simulate the flowfield around delta wings. For example, static flowfields around delta wings were calculated by Fujii and Schiff,[5]

Received 19 March 2002; revision received 13 July 2003; accepted for publication 5 August 2003.

*Graduate Research Assistant, Department of Aerospace Engineering; currently Research Engineer, Korea Aerospace Research Institute, Taejon, Republic of Korea.

†J. L. Constant Distinguished Professor, Department of Aerospace Engineering. Associate Fellow AIAA.

Hartwich and Hsu,[6] and Ekaterinaris et al.[7] by using the thin-layer Navier–Stokes equations. For roll-oscillating delta wings, thin-layer Navier–Stokes solvers were used by Kandil and Chuang[8] and Chaderjian and Guruswamy[9] as well. To the authors' knowledge, few numerical solutions have been reported using full Navier–Stokes solvers on pitching delta wings, particularly inside a wind tunnel. The full Navier–Stokes solver is expected to better predict the flowfield in the separated flow and vortex-bursting regions.

For validation of the numerical predictions, accurate experimental data are necessary. However, the experimental data with which comparison is made are taken inside wind tunnels, where several factors affecting the accuracy need to be evaluated and treated correctly.[10] Among these factors the wall interference effect is important, particularly for a configuration with strong vortex flow in the presence of solid tunnel walls. The presence of solid walls is to increase the overall effective geometric angle of attack, to change the streamline curvature, to alter the local angles of attack, and to increase the dynamic pressure over the test model because of blockage.[10] The existing correction methods of wall interference are summarized in Ref. 10. However, wind-tunnel wall interference in unsteady tests has not been as thoroughly investigated as that in steady tests. To simulate static test environments, Thomas and Lan[11] and Hsing and Lan[12] employed thin-layer Navier–Stokes solutions. Calculated static pressure distributions on the tunnel walls were used to compute the wake blockage and upwash corrections for the model aerodynamics. However, in unsteady testing, additional effects must be accounted for such as the reflection of model-generated disturbances by the wall, the oscillatory wake of the model, and so on.[10]

For two-dimensional subsonic flow, Bland[13] derived an integral equation relating the downwash to the induced unsteady pressure jump at the airfoil. The downwash was simply prescribed as one with simple harmonic variation. The results showed unsteady wall effects in the case of tunnel resonance. Unsteady tunnel-wall pressure distributions were computed by Kuczka[14] with three-dimensional image vortex methods. The corrected results of both ventilated and closed walls agreed well only at low angles of attack. Three-dimensional transonic small disturbances computations on pitching rectangular wings in a transonic wind tunnel were performed by Seebass et al.[15] These aforementioned methods are not applicable for configurations with vortex-separated flow.

Measured unsteady wall-pressure distributions during a dynamic test can be used to correct the wall-induced unsteady pressure data at the model. Panel methods for small-amplitude oscillating models are described in Ref. 10. The velocity potential and the dipole strength for the wall-induced pressure on the airfoil can be obtained from a measured unsteady pressure distribution on the tunnel wall.

In this paper, three-dimensional unsteady full Navier–Stokes solutions are employed to investigate the unsteady wall-interference effects for pitching delta wings in a wind tunnel. The computed wall static pressure distributions and their variations with time are saved in the form of Fourier series to reduce the necessary data storage. These data can be used to display the wall-pressure variation during testing through dynamic animation and to compute the interference flowfield as well.

Numerical Schemes

A three-dimensional unsteady Reynolds-averaged full Navier–Stokes solver in conservation form will be used to compute the flowfield around pitching delta wings. An existing steady-state thin-layer Navier–Stokes code, KUNS3D, is modified to perform the unsteady computations with moving grids. The KUNS3D code is a modified version of ARC3D[16] for the computation of tunnel interference effects in static testing.

Governing Equations

Written in generalized curvilinear coordinates, the present method solves the following unsteady full Navier–Stokes equations:

$$\boldsymbol{Q}_t + \boldsymbol{E}_\xi + \boldsymbol{F}_\eta + \boldsymbol{G}_\zeta = \boldsymbol{E}_{v_\xi} + \boldsymbol{F}_{v_\eta} + \boldsymbol{G}_{v_\zeta} \tag{1}$$

where

$$\boldsymbol{Q} = J^{-1}\begin{bmatrix}\rho\\ \rho u\\ \rho v\\ \rho w\\ e\end{bmatrix}, \qquad \boldsymbol{E} = J^{-1}\begin{bmatrix}\rho U\\ \rho uU + \xi_x p\\ \rho vU + \xi_y p\\ \rho wU + \xi_z p\\ U(e+p) - \xi_t p\end{bmatrix} \tag{2}$$

$$\boldsymbol{F} = J^{-1}\begin{bmatrix}\rho V\\ \rho uV + \eta_x p\\ \rho vV + \eta_y p\\ \rho wV + \eta_z p\\ V(e+p) - \eta_t p\end{bmatrix}, \qquad \boldsymbol{G} = J^{-1}\begin{bmatrix}\rho W\\ \rho uW + \zeta_x p\\ \rho vW + \zeta_y p\\ \rho wW + \zeta_z p\\ W(e+p) - \zeta_t p\end{bmatrix} \tag{3}$$

where $\boldsymbol{Q}$ is the solution vector and $\boldsymbol{E}, \boldsymbol{F}, \boldsymbol{G}$ are the inviscid flux vectors. The detailed expressions of the viscous flux vectors $\boldsymbol{E}_v, \boldsymbol{F}_v$ and $\boldsymbol{G}_v$ can be found in Ref. 17 (pp. 326–330). The flux vectors are linearized in time about $\boldsymbol{Q}^n$ by using a Taylor series:

$$\Delta\boldsymbol{Q}^n = \frac{\vartheta\,\Delta t}{1+\varphi}\frac{\partial}{\partial t}(\Delta\boldsymbol{Q}^n) + \frac{\Delta t}{1+\varphi}\frac{\partial}{\partial t}\boldsymbol{Q}^n + \frac{\varphi}{1+\varphi}\Delta\boldsymbol{Q}^{n-1} + O\left[\left(\vartheta - \frac{1}{2} - \varphi\right)\Delta t^2 + \Delta t^3\right]$$

$$\Delta\boldsymbol{Q}^n = \boldsymbol{Q}^{n+1} - \boldsymbol{Q}^n \tag{4}$$

where the parameters φ and ϑ are chosen to be $\frac{1}{2}$ and 1, respectively, for a second-order formulation in unsteady computation. The flux vectors ($\boldsymbol{E}$, $\boldsymbol{F}$, etc.) are linearized in time about $\boldsymbol{Q}^n$ by a Taylor series such that

$$\boldsymbol{E}^{n+1} = \boldsymbol{E}^n + A^n\Delta\boldsymbol{Q}^n + O(h^2) \tag{5}$$

where A is the flux Jacobian of $\boldsymbol{E}$. Substituting Eqs. (4) and (5), and similar expressions for other flux vectors, into Eq. (1), with central-difference schemes applied to all space derivatives, the resulting vector equations can be approximately factorized[16,17] to the following form. For simplicity, only the first-order formulation is shown ($\varphi = 0$, $\vartheta = 1$):

$$\left(I + h\delta_\xi A^n - hRe^{-1}\delta_\xi J^{-1}L^n\right)\left(I + h\delta_\eta B^n - hRe^{-1}\delta_\eta J^{-1}M^n\right) \times \left(I + h\delta_\zeta C^n - hRe^{-1}\delta_\zeta J^{-1}N^n\right)\Delta\boldsymbol{Q}^n = -h\left(\delta_\xi\boldsymbol{E}^n + \delta_\eta\boldsymbol{F}^n + \delta_\zeta\boldsymbol{G}^n - Re^{-1}\left(\delta_\zeta\boldsymbol{E}_v^n + \delta_\eta\boldsymbol{F}_v^n + \delta_\zeta\boldsymbol{G}_v^n\right)\right) \tag{6}$$

where δ is the central difference operator and its subscript represents differentiation with the curvilinear coordinates as indicated. Other symbols are defined in the Nomenclature. The left-hand side of Eq. (6) involves the product of three large block tridiagonal matrices and is called the implicit part of the algorithm. These block tridiagonal matrix equations are solved for the unknowns, $\Delta\boldsymbol{Q}^n$, by block lower–upper decomposition using locally one-dimensional matrix inversions. In ARC3D, this equation is simplified to a scalar pentadiagonal form for steady-state computations with first-order time accuracy.

In unsteady flow, second-order time-accurate methods are needed. The flowfield is first computed for the static solution and then integrated forward in time. The implicit viscous terms in Eq. (6) can be ignored without affecting the accuracy to save computing time.[16] By ignoring all viscous flux Jacobians L, M, N on the left-hand side of Eq. (6), the second-order approximate factorized alternate direction implicit scheme can be written as follows:

$$\left(I + \tfrac{2}{3}h\delta_\xi A^n\right)\left(I + \tfrac{2}{3}h\delta_\eta B^n\right)\left(I + \tfrac{2}{3}h\delta_\zeta C^n\right)\Delta\boldsymbol{Q}^n = \tfrac{1}{3}\Delta\boldsymbol{Q}^{n-1} - \tfrac{2}{3}h\left(\delta_\xi\boldsymbol{E}^n + \delta_\eta\boldsymbol{F}^n + \delta_\zeta\boldsymbol{G}^n - Re^{-1} \times \left(\delta_\zeta\boldsymbol{E}_v^n + \delta_\eta\boldsymbol{F}_v^n + \delta_\zeta\boldsymbol{G}_v^n\right)\right) \tag{7}$$

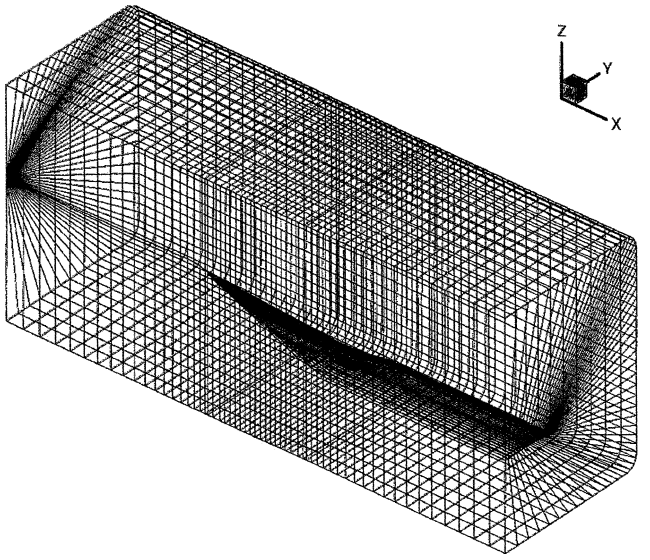

Fig. 1 A grid system for a 70-deg delta wing in a wind tunnel.

For the viscous-separated and/or bursting vortical flowfields, the full Navier–Stokes equations, as opposed to the thin-layer approximation, are better for improved resolution of all flowfield characteristics. This means that all the viscous terms associated with the ξ and η derivatives are retained in the equations in addition to the ζ derivatives.

To assure the numerical stability, Jameson's artificial dissipation terms are added to the algorithm without affecting the accuracy of physical viscous effects.[18] In addition, the algebraic turbulence model of Balwin and Lomax of the original ARC3D code is retained.[16]

Grid Systems

The body-conforming grid systems of a delta wing in a tunnel and free air are based on an O-H mapping using an algebraic grid generator. For a symmetric case under consideration, only half of the domain is modeled and computed as shown in Fig. 1.

To simulate a delta wing in pitching motion, a new grid system at every time step in integration is needed. The new grid system is generated by allowing the existing grid system to move with the motion of the wing surface. The initial grid system is generated at a fixed angle of attack and used to compute the steady-state solution. During dynamic computation, the surface grids are moved according to the prescribed angular velocity of model oscillation. The grid speed is allowed to decay along the normal distance to zero at the outer boundary. The grid speeds are also explicitly obtained in the process. The method consists of two major steps:

1) Compute the grid speeds at $\zeta = 0$ (i.e., the solid surface and the wake surface) from the prescribed grid locations and movements.

2) Compute the flowfield grid locations, $\zeta > 0$, from the grid speeds. The grid speed does not change along the y direction.

These two steps are described in detail as follows.

In step 1, Grid points of the solid surface and the wake portion of $\zeta = 0$ are translated and rotated as defined by the sinusoidal motion

$$\alpha = \alpha_o + \alpha_{\text{amp}} \sin \omega t$$

$$x = (x_o - x_{\text{center}}) \cos\left(f_1^5 \alpha\right) + (z_o - z_{\text{center}}) \sin\left(f_1^5 \alpha\right) + x_{\text{center}}$$

$$z = -(x_o - x_{\text{center}}) \sin\left(f_2^5 \alpha\right) + (z_o - z_{\text{center}}) \cos\left(f_2^5 \alpha\right) + z_{\text{center}} \tag{8}$$

where x and z, nondimensionalized by the root chord length, are the surface grid coordinates during the pitching motion and x_o and z_o are the initial grid locations. Subscript center denotes the axis or center of rotation of the model; α_o is the mean angle of attack for the pitching motion and α_{amp} is the amplitude. The parameters f_1 and f_2 are the weighting factors.

In Eq. (8), the weighting factors are defined such that the far-field portion is rotated by a lesser amount compared to the model surface rotation. This will ensure the physical constraints of the wake. By a trial-and-error method to avoid a negative Jacobian (J), the weighting factors are determined as follows:

$$\text{If } d > 1 - x_{\text{center}}, \qquad f_1 = 0$$

$$f_2 = 1 - \tanh\left[\frac{d - (1 - x_{\text{center}})}{8.999}\right]$$

$$\text{If } d \le 1 - x_{\text{center}}, \qquad f_1 = f_2 = 1 \tag{9}$$

where d is the nondimensionalized distance of the grid points from the center of rotation.

The surface grid speeds x_t and z_t are then calculated as the algebraic difference of the two grid locations in x and z divided by the elapsed time Δt. The next task is to determine the coordinate locations of all other grid points in the field.

In step 2, the flowfield grid speeds are calculated as fractions of the surface grid speeds. The fraction is defined as f_3:

$$f_3 = \frac{(\zeta_{\max})^5 - \zeta^5}{(\zeta_{\max})^5} \tag{10}$$

where the subscript max denotes the maximum grid number in the ζ direction (i.e., normal to the surface).

Finally, the new coordinates of the field grid points are then obtained algebraically from the grid speeds:

$$x^{n+1} = x^n + (x_t)(\Delta t), \qquad y^{n+1} = y^n$$

$$z^{n+1} = z^n + (z_t)(\Delta t) \tag{11}$$

As mentioned earlier, the grid speed along the y coordinate is zero.

Dual Time Subiteration

The dual time subiteration presented here is based on the CFL3D method of NASA Langley Research Center. The subiteration scheme is to ensure that after one time step additional iterations are performed at this new time step before integrating to the next time step. This is accomplished by using a pseudotime (τ) iteration. Adding a pseudotime term, we replace the first term of Eq. (1) with the left-hand side of Eq. (12):

$$\frac{1}{J}\frac{\partial \boldsymbol{Q}}{\partial \tau} + \frac{(1+\phi)(\boldsymbol{Q}^{n+1} - \boldsymbol{Q}^n) - \phi(\boldsymbol{Q}^n - \boldsymbol{Q}^{n-1})}{J \Delta t} = R(\boldsymbol{Q}^{n+1}) \tag{12}$$

where R represents all other terms in Eq. (1) except the first one. Equation (12) is then discretized and iterated in m, where m is the subiteration number:

$$\left[\left(\frac{1+\phi'}{J\Delta\tau} + \frac{1+\phi}{J\Delta t}\right) I + \delta_\xi A^m + \delta_\eta B^m + \delta_\zeta C^m\right] \Delta \boldsymbol{Q}^m$$

$$= \frac{\phi' \Delta \boldsymbol{Q}^{m-1}}{J\Delta\tau} + \frac{\phi \Delta \boldsymbol{Q}^{n-1}}{J\Delta t} - \frac{(1+\phi)(\boldsymbol{Q}^m - \boldsymbol{Q}^n)}{J\Delta t} + R(\boldsymbol{Q}^m) \tag{13}$$

$$\boldsymbol{Q}^{m+1} = \boldsymbol{Q}^m + \Delta \boldsymbol{Q}^m \tag{14}$$

As m goes to infinity in Eq. (13), the pseudotime term vanishes if the subiterations converge and, eventually, $\boldsymbol{Q}^{m+1}$ becomes $\boldsymbol{Q}^{n+1}$. In

practice, just a few subiterations are enough for a converged solution. By using the alternate direction implicit (ADI) scheme with the first-order pseudotime accuracy ($\phi' = 0$), the equations are solved as a series of sweep in each direction. It is difficult to find an optimal value of $\Delta\tau$, because convergence is improved continuously and slowly as $\Delta\tau$ increases. However, it is known that a very large $\Delta\tau$ may make the scheme unstable. The quantity $\Delta\tau$ is usually 10^4–10^5 times the physical time step, Δt. A value of $\Delta\tau$ equal to 100 is used in the present investigation.

Boundary Conditions

On the body surface, the no-slip condition must be satisfied in a viscous flowfield. To satisfy this condition, the contravariant velocities U, V, and W are set to zero on the solid surface. For a model in free air, at the lateral boundary of the domain used in the analysis, a nonreflective boundary condition is used. That is, if the computed normal velocity to the boundary is outward, momentum fluxes from inside are allowed to propagate outward to change the conditions at the interface. The locally one-dimensional Riemann invariant boundary condition is used at the inlet. For the outlet boundary conditions, flow variables are extrapolated from the interior except for the pressure, which is specified.[16]

For the model inside a tunnel, two grid blocks are constructed: one to wrap around the model (called the inner block) and the other near the tunnel walls (called the outer block). These two blocks are overlapped by one layer of grid points. In this case, the boundary conditions at the interface for one block are directly injected from the interior of the other block.[9]

For the interference flowfield computation, the solid model is removed from inside the tunnel without changing the grid system. Therefore, continuity of the flowfield through the original model location must be imposed, while the far-downstream boundary conditions are fixed to the freestream properties, except for the pressure, which remains to be as specified. Computed wall-pressure distributions are specified on the tunnel-wall surface.

Thomas and Lombard[19] pointed out the need to maintain global conservation on moving grids. Geometric conservation law is essential for moving grids. The main feature in a dynamic grid system is the calculation of contravariant velocity components when the grid speeds (ξ_t , η_t, and ζ_t) are not zero.

Considering the continuity equation in a motionless (u, v, and $w = 0$) flowfield,

$$(1/J)_t + (\xi_t/J)_\xi + (\eta_t/J)_\eta + (\zeta_t/J)_\zeta = 0 \tag{15}$$

This is the continuity equation that should be satisfied in the whole flowfield at any time. If the grid systems are also motionless, $\xi_t = \eta_t = \zeta_t = 0$; thus, $J = \text{const}$ is the natural result of Eq. (15). But it is difficult to satisfy the preceding equation for the moving grid systems because of the discretization errors. Thus, for the moving grid systems, Eq. (15) should also be satisfied at all times to eliminate the errors caused by the grid cell movement and distortion. To satisfy Eq. (15), the Jacobian J at the next time level is explicitly evaluated using the values of the current time level as follows:

$$J^{n+1} = \left\{1/J^n - \Delta t[(\xi_t)_\xi + (\eta_t)_\eta + (\zeta_t)_\zeta)^n\right\}^{-1} \tag{16}$$

In this paper, the preceding equation is discretized with forward differencing in time and central differencing in space.

Wall-Pressure Representation by Fourier Series

Because the computed wall pressure at each grid point varies with time, and the time step is small, it would require a large storage space to store these data for processing. One solution to this problem is to use a Fourier series representation. Assume $C_p(t)$ is defined in the interval $C < t < C + T$ and approximated by a Fourier series,

$$C_p(t) = a_0/2 + [a_1 \cos(\pi t/T) + a_2 \cos(2\pi t/T) + b_1 \sin(\pi t/T) + b_2 \sin(2\pi t/T)] \tag{17}$$

where

$$a_n = \frac{1}{T}\int_C^{C+2T} Cp(t) \cos\frac{n\pi t}{T}\,\mathrm{d}t$$

$$b_n = \frac{1}{T}\int_C^{C+2T} Cp(t) \sin\frac{n\pi t}{T}\,\mathrm{d}t$$

Numerical integration can be done easily using the trapezoidal rule for these Fourier coefficients. Instead of the huge wall-pressure data file, Fourier coefficients are stored and used in an Euler resimulation process as the wall boundary conditions. This idea should also be useful in a direct measurement of tunnel-wall pressure in dynamic testing.

Wall-Pressure Signature Method

The correction technique used in the present investigation is based on the calculated tunnel-wall pressure distribution. The wall-pressure distribution obtained from the Navier–Stokes computation is used as the boundary condition for an Euler resimulation of the tunnel domain without the model. This process produces an interference flowfield that contains the change in upwash, $\Delta\alpha$, and the actual dynamic pressure q_c at the model to correct the measured forces and moments. For this resimulation process, the wall pressure is the only variable specified on the outer boundary of the tunnel flowfield. Therefore, the tunnel-wall boundary becomes a force-free transpiration boundary.

With the upwash and dynamic pressure information obtained in the tunnel domain, the correct angle of attack can be determined using the velocity changes:

$$\alpha_c = \alpha + \Delta\alpha \tag{18}$$

where

$$\Delta\alpha = \tan^{-1}\frac{\Delta w}{U_\infty + \Delta u}$$

The correction to dynamic pressure for the blockage effect is determined from

$$\frac{q_c}{q_\infty} = \frac{\left\lfloor (U_\infty + \Delta u)^2 + \Delta w^2 \right\rfloor}{U_\infty^2} \tag{19}$$

Both the upwash and blockage corrections are determined by averaging these values on the whole wing surface location in the interference flowfield.

The measured (or computed in the present case) force and moment coefficients are first corrected for the blockage effect as follows:

$$C_L = L/q_c S, \qquad C_D = D/q_c S, \qquad C_m = M/q_c S\bar{c} \tag{20}$$

These coefficients are then taken to be the values at the corrected angle of attack α_c instead of the indicated α.

Results and Discussion

Test Models

For code validation, two sets of test data are used for comparison. The first one is that of Ref. 1 for a 70-deg delta wing, 18 in. long with chamfered edges; the tunnel size is 4 ft wide and 3 ft high. The test Reynolds number was 1×10^6 (based on the wing root chord). Pitching moments were taken at 50% wing root chord. The second set of data is from Ref. 20 for a 70-deg delta wing, 18 in. long with beveled edges, and the data were obtained in NASA Langley's 12-ft low-speed wind tunnel. The Reynolds number was 0.4 million per foot. Center of rotation and pitching moment were taken at 40% mean

Table 1 Values for dynamic computations

Case	K	α_{mean}, deg	α_{amp}, deg
Code validation	0.0376	27.0	17.0
1[a]	0.167	20.0	5.0
2[b]	0.067	20.0	5.0
3[c]	0.167	20.0	10.0

[a]Reference. [b]Low frequency. [c]Large amplitude.

aerodynamic chord. For all other calculations, the model and wind tunnel are those of Ref. 3. The 70-deg delta wing, in a wing–fuselage combination, is constructed of a flat plate (0.024 thickness-to-chord ratio) with sharp beveled leading and trailing edges. The tunnel test section is 5 ft wide, 3 ft high, and 8 ft long. The root chord length of the model was 20.61 in. The Mach number was estimated to be 0.14 and the Reynolds number 1×10^6 (based on the root chord length). In the analysis, the streamwise domain is set to five root chord lengths with $60 \times 62 \times 50$ gridlines in the streamwise, circumferential, and normal directions, respectively, unless indicated otherwise. For the dynamic computations, four cases are computed in free air and in the wind tunnel of Ref. 3. These four cases are shown in Table 1.

For code validation, computed results are referenced to the same center of pitching moment as the experimental results. For cases 1 through 3, 25% root chord location is the center of pitching moment.

Code Validation

In Fig. 2, the computed static data are compared to the wind-tunnel measurements of Ref. 1. The results show good agreement for C_L and C_D with Wentz's experiments, even beyond the angle of attack where the vortex breakdown occurs. According to Ref. 1, vortex breakdown occurs at the trailing edge at $\alpha = 30$ deg, in agreement with the present computation. The pitching moment coefficient shows a larger discrepancy, perhaps because the computed leading-edge vortices are more outboard with the wing tip more loaded than the measured data showed. In Fig. 2, additional results with grid-line numbers of $70 \times 72 \times 50$, $60 \times 75 \times 50$, and $60 \times 62 \times 62$ are also presented. It appears that the effect of grid size on the predicted aerodynamic characteristics is small except for the pitching moment coefficient at high angles of attack. Because the focus of the present computation is the pressure distribution on the tunnel wall (i.e., the far-field disturbances), inaccuracy in predicting the magnitude of pitching moment coefficient, which depends mainly on the near-field pressure distribution, should not significantly affect the calculation of wall interference corrections. It should be noted that the data of Ref. 1 have already been corrected for wall interference, the magnitude of which is unknown but expected to be small.[11,12] The computed static normal force coefficients are also compared with those in Ref. 20. Figure 3 shows that the computed normal force coefficients are significantly higher than the experimental data. Instead of speculating on a possible reason for the discrepancy, it should be noted that the present computed normal force coefficients also agree reasonably well with the test data of Ref. 3, although the test configuration in Ref. 3 included a fuselage. In the test data of Ref. 20, vortex breakdown at the trailing edge was determined to occur at $\alpha = 22.5$ deg, compared with 30 deg in Ref. 1. However, only Ref. 20 was found to contain dynamic test data of a delta wing alone in large-amplitude oscillation.

In the dynamic computation, the case with $k = 0.0376$, $\alpha_{mean} = 20$ deg, and $\alpha_{amp} = 5$ deg is used to check the algorithm. One and a half cycles appear to be sufficient to get a converged solution. With a nondimensionalized time step of 0.007 ($= ta_\infty / C_r$), this corresponds to 40,000 time steps and about 500 h of CPU time is required on an SGI Origin 2400 400-MHz single processor. At each time step, 5 subiterations are performed, with 10 subiterations for angles of attack higher than 30.0 deg. Using this same process, the dynamic aerodynamic coefficients for the configuration of Ref. 20 are calculated and presented in Fig. 4. Although the computed dynamic normal force coefficients are higher than the test data, similar to the static results, the main

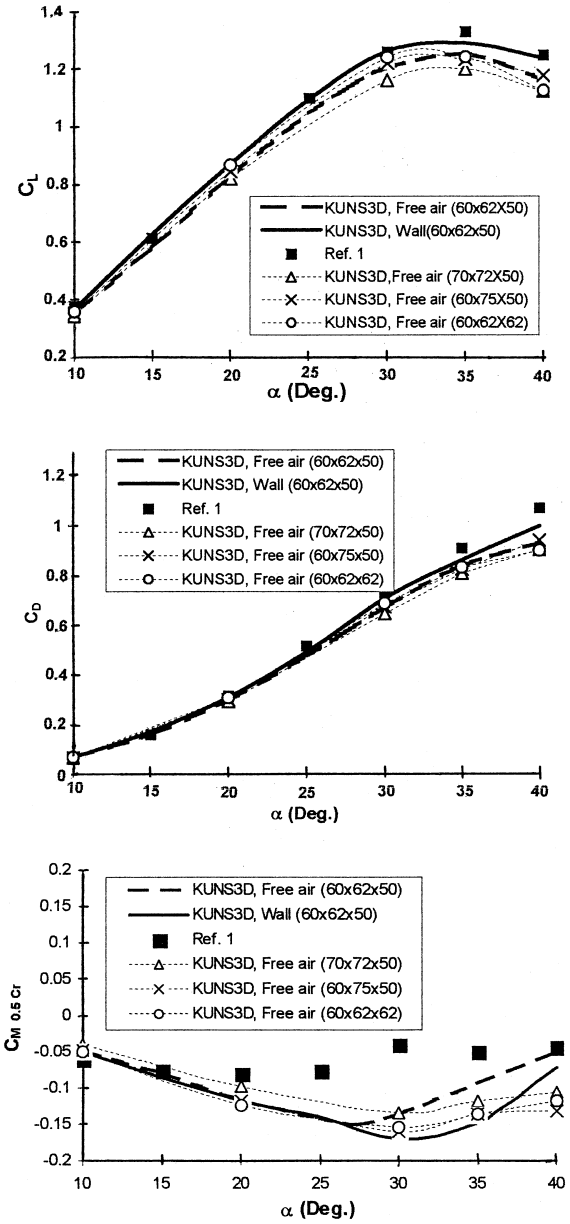

Fig. 2 Comparison of computed static aerodynamics with data for a 70-deg delta wing at $Re = 10^6$ and $M_\infty = 0.2$.

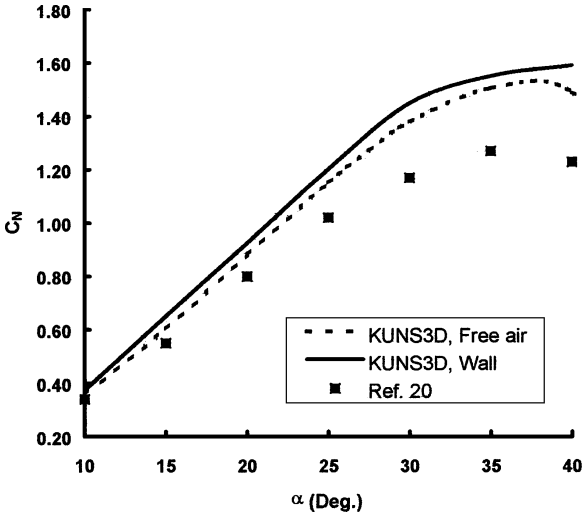

Fig. 3 Comparison of computed normal force coefficient for a 70-deg delta wing with data at $Re = 10^6$ and $M_\infty = 0.2$.

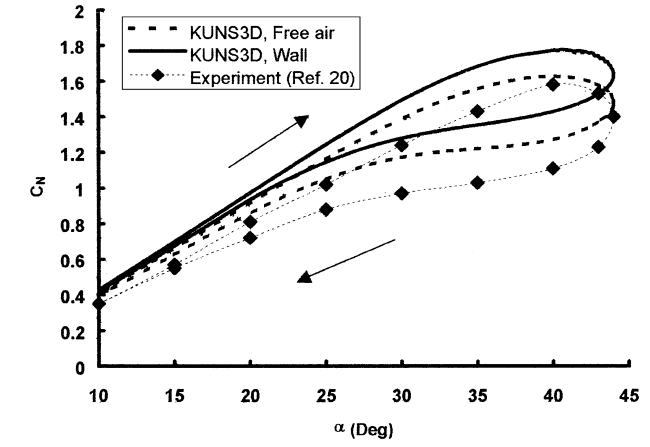

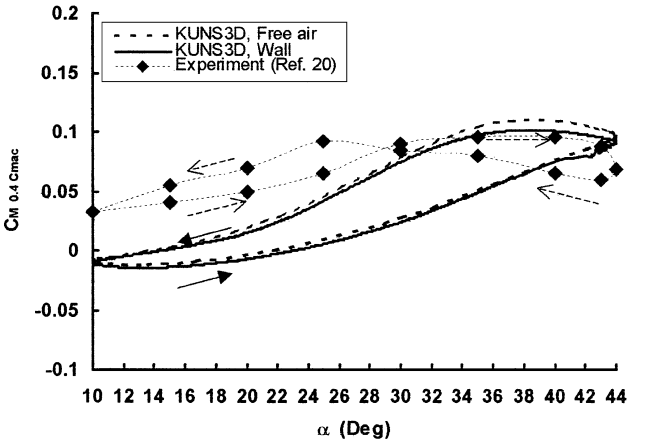

Fig. 4 Comparison of computed dynamic aerodynamics for a 70-deg delta wing with data at $Re = 10^6$, $M_\infty = 0.2$, $k = 0.0376$, and $\alpha = 27 \pm 17$ deg.

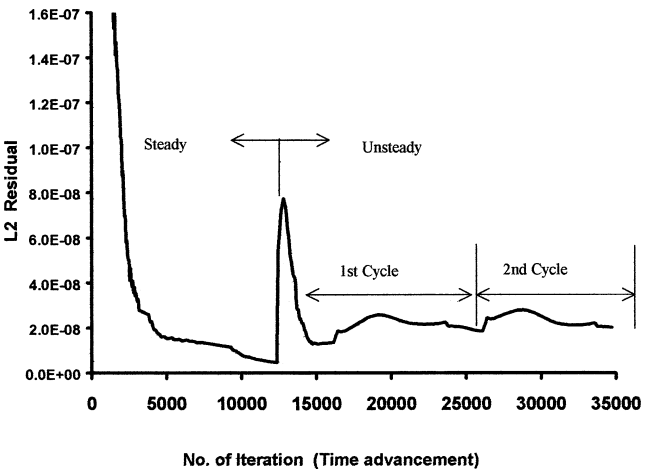

Fig. 5 Time history of numerical residuals.

purpose here is to show that the computed hysteresis loops of C_N are similar. Figure 5 indicates good convergence history of the numerical residuals in both static and dynamic computations. The magnitude of residuals is to indicate how well the Navier–Stokes equations are satisfied and the L2 residual is the square root of the average of sum of squared residuals over all grid points.

In Figs. 6 and 7, the computed wall-pressure distributions are presented. Lower pressure develops on the top surface of the tunnel wall, whereas higher pressure exists on the bottom surface. During downstroke the wall pressure tends to be more positive everywhere than during upstroke at the same angles of attack.

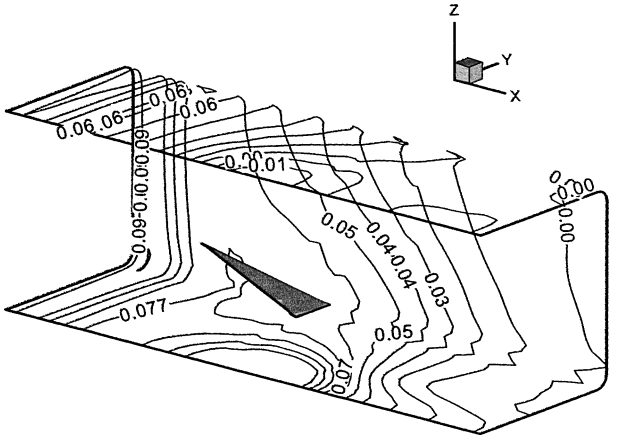

Fig. 6 Computed wall-surface pressure distribution at $\alpha = 25$ deg in upstroke for a 70-deg delta wing in tunnel at $Re = 10^6$, $M_\infty = 0.2$, $k = 0.0376$, and $\alpha = 27 \pm 17$ deg.

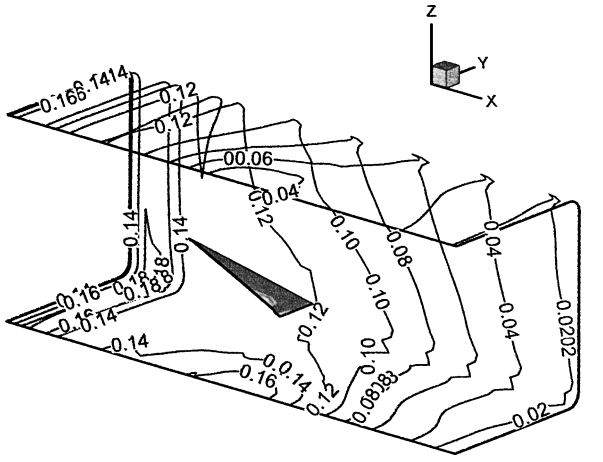

Fig. 7 Computed wall-surface pressure distribution at $\alpha = 25$ deg in downstroke for a 70-deg delta wing in tunnel at $Re = 10^6$, $M_\infty = 0.2$, $k = 0.0376$, and $\alpha = 27 \pm 17$ deg.

Evaluation of Wall Effects on Aerodynamics

As pointed out in Ref. 20, as the reduced frequency and amplitude of oscillation are increased the hysteresis is enhanced. Also, the model in the tunnel develops higher lift and drag coefficients. The computed results for those three cases mentioned earlier are analyzed in the following. It should be noted that in practice the theoretically derived correction factors are applied to the measured, not computed, aerodynamic coefficients.

Case 1 ($k = 0.167$, $\alpha_{\text{mean}} = 20$ deg, $\alpha_{\text{amp}} = 5$ deg) is one of the three cases presented in Figs. 8–10. It is of interest to estimate how the leading-edge vortex strength is affected by the presence of the tunnel wall. The total pressure coefficients (C_{po}) in the vortex core at the trailing-edge location are compared in Fig. 8. A more negative C_{po} implies a vortex with higher circulation. It is seen that a model in the wind tunnel develops a stronger leading-edge vortex than that in the free air. However, the vortex position, not shown, does not show significant difference at the same α in both upstroke and downstroke. To obtain the wall-interference corrections, the interference flowfields are first computed by solving the Euler equations with the wall-pressure distributions as the forcing function. To find the correction factors for the total forces and moment, weighted averages over the whole wing surface location are computed and presented in Fig. 9 for both the upwash and blockage (in dynamic pressure ratios) corrections. Upwash correction is about 1.21 deg and the blockage

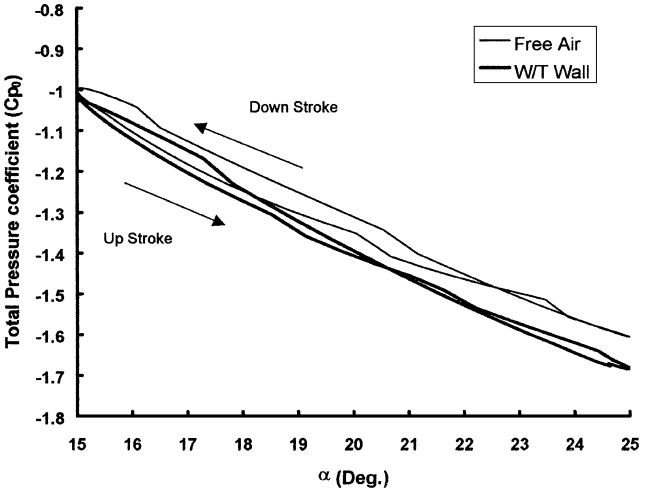

Fig. 8 Vortex strength variation for a 70-deg delta wing in dynamic motion in a 3 × 5 ft tunnel at $Re = 10^6$, $M_\infty = 0.2$, $k = 0.167$, and $\alpha = 20 \pm 5$ deg (case 1).

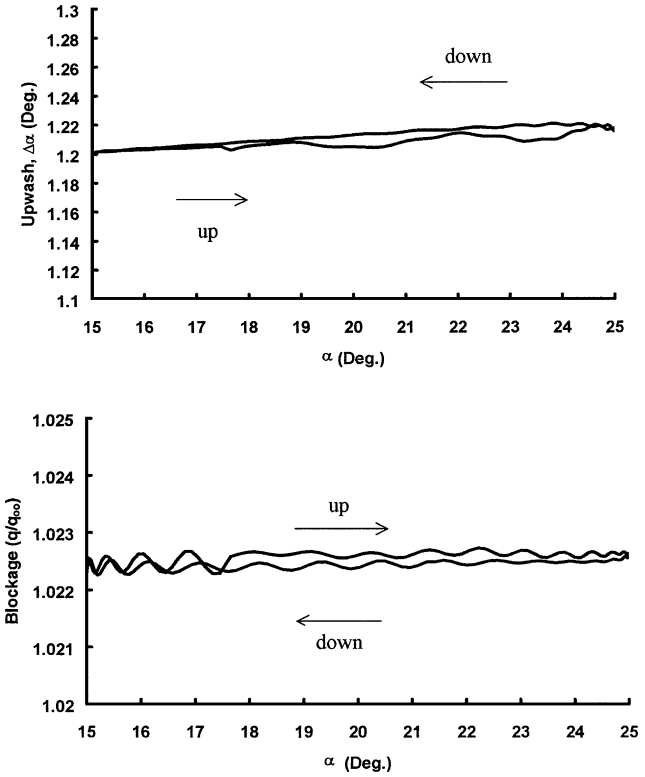

Fig. 9 Blockage and upwash corrections for a 70-deg delta wing in a 3 × 5 ft tunnel at $Re = 10^6$, $M_\infty = 0.2$, $k = 0.167$, and $\alpha = 20 \pm 5$ deg (case 1).

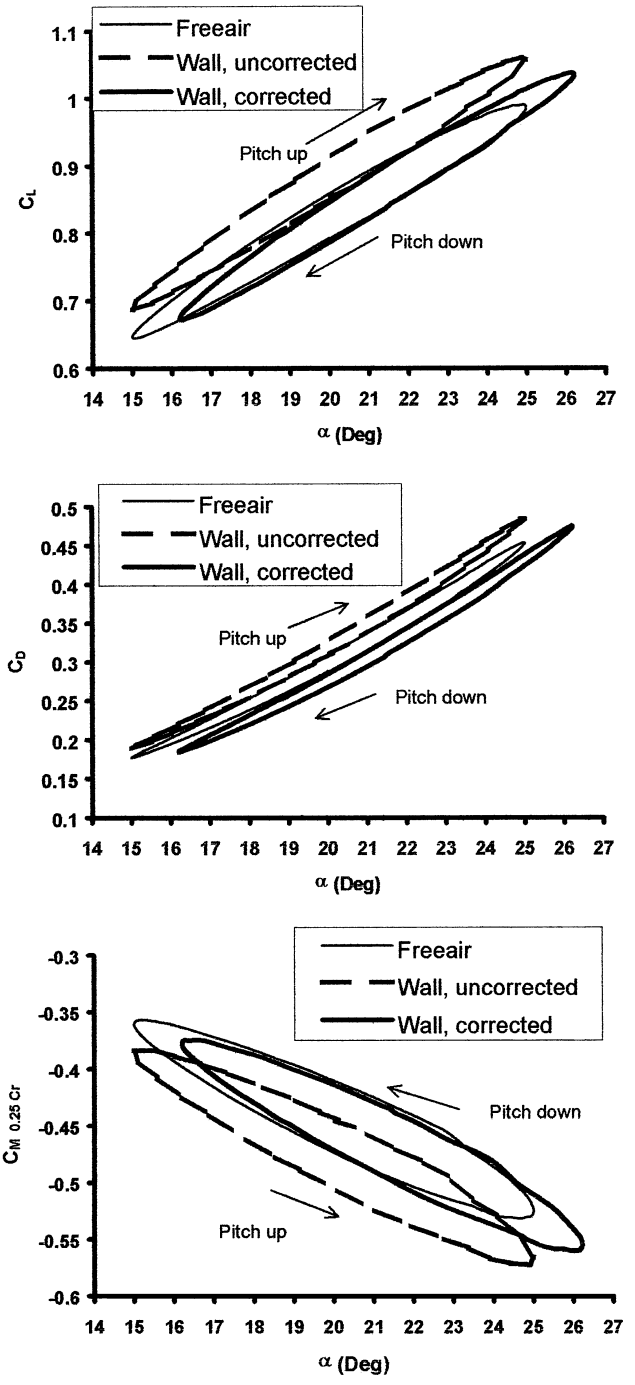

Fig. 10 Corrected aerodynamics for a 70-deg delta wing in a 3 × 5 ft tunnel at $Re = 10^6$, $M_\infty = 0.2$, $k = 0.167$, and $\alpha = 20 \pm 5$ deg (case 1).

correction is about 1.0225 at $\alpha = 20$ deg in the tunnel. Both upwash and blockage corrections show some hysteresis. The corrected force and moment coefficients are presented in Fig. 10. It is seen that the corrected C_L and C_m agree well in slopes and magnitudes of the hysteresis loops with the computed free-air results; however, C_D is overcorrected.

In the remaining illustration of wall-interference corrections, only the lift coefficient will be presented. More detailed results are available in Ref. 21. In Fig. 11, C_L for case 2 ($k = 0.067$, $\alpha_{\text{mean}} = 20$ deg, $\alpha_{\text{amp}} = 5$ deg) is shown. As in case 1, the model in the tunnel again develops higher lift coefficients. However, the amount of hysteresis is much less because the reduced frequency is much lower. The upwash correction is about 1.07 deg and the blockage correction is about 1.017 at $\alpha_{\text{mean}} = 20$ deg. The correction factors (not shown) have only small hysteresis. Therefore, at low reduced frequencies, static correction factors should be sufficient in dynamic testing. Again, the corrected tunnel C_L shows good agreement with the computed free-air results.

Finally, the computed results for case 3 with a large amplitude and high frequency ($k = 0.167$, $\alpha_{\text{mean}} = 20$ deg, $\alpha_{\text{amp}} = 10$ deg) in the tunnel and free air are compared in Fig. 12. It is seen that the model in the tunnel shows higher C_L and significant increase in slopes with the angle of attack than in the free air. The amount of hysteresis is also increased. The upwash correction is 1.4 deg and the blockage correction is 1.027 at $\alpha_{\text{mean}} = 20$ deg in the tunnel. The results might be slightly overcorrected because the computed vortex bursting characteristics in free air are different from those in the tunnel. Note that the wind-tunnel data are regarded as "uncorrectable" if the flow physics, such as the extent in flow

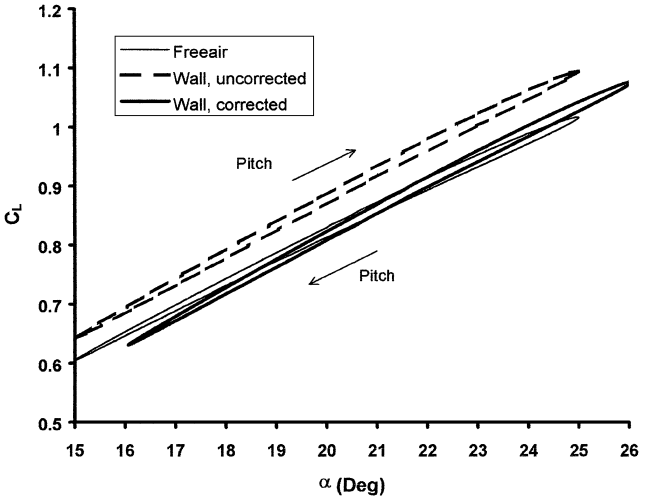

Fig. 11 Corrected aerodynamics for a 70-deg delta wing in a 3 × 5 ft tunnel at $Re = 10^6$, $M_\infty = 0.2$, $k = 0.067$ and $\alpha = 20 \pm 5$ deg (case 2).

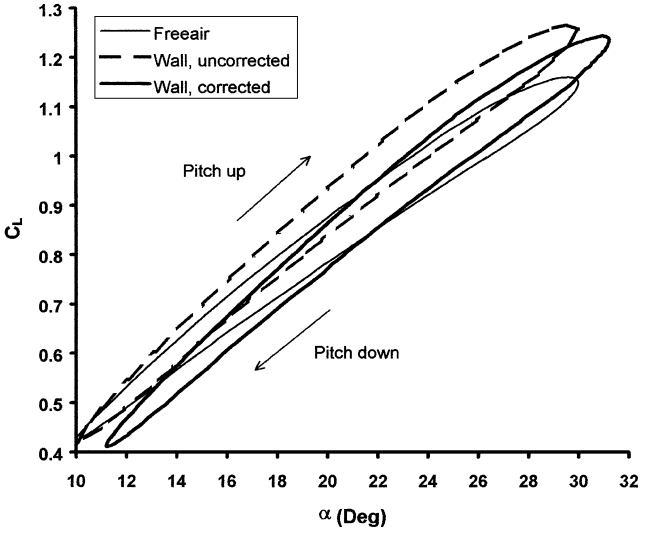

Fig. 12 Corrected aerodynamics for a 70-deg delta wing in a 3 × 5 ft tunnel at $Re = 10^6$, $M_\infty = 0.2$, $k = 0.167$, and $\alpha = 20 \pm 5$ deg (case 3).

separation, vortex bursting, and so forth, are changed because of the wall interference.

Conclusions

A numerical method for the analysis of tunnel-wall interference effects in forced-oscillation testing was presented. The wall-pressure field was computed by using an unsteady three-dimensional full Navier–Stokes solver with dynamic grid systems for a 70-deg pitching delta wing in the wind tunnel. The computed wall-pressure field was then imposed as a boundary condition for Euler resimulation to obtain the interference flowfield.

The calculated static results were in good agreement with the experimental data of Wentz. The computed hysteresis loop of the normal force coefficient for a pitching delta wing with $k = 0.0376$, $\alpha_{\text{mean}} = 27$ deg, and $\alpha_{\text{amp}} = 17$ deg was shown to be similar to the dynamic test data. The wall-interference effect on the vortex strength, as indicated by the total pressure inside the vortex core at the trailing edge, showed a trend similar to the upwash corrections on the aerodynamic coefficients. Analysis of the wall-induced blockage and upwash corrections on the model aerodynamics were conducted with various oscillation amplitudes and reduced frequencies. For the case with a larger amplitude and reduced frequency, flow hysteresis and wall-interference effects were also greater. The longitudinal aerodynamic coefficients for a model in the tunnel were corrected based on the wall-pressure signature concept using the computed wall-pressure distribution. The corrected results showed good agreement in the slope and magnitude of the hysteresis loops with the computed results in free air, except at low angles of attack with a large oscillation amplitude and high frequency employed in the computation.

Acknowledgment

This research was supported by the Kansas Center for Advanced Scientific Computing at the University of Kansas.

References

[1]Wentz, W. H., and Kohlman, D. L., "Vortex Breakdown on Slender Sharp-Edged Wings," *Journal of Aircraft*, Vol. 8, No. 3, 1971, pp. 156–161.

[2]Wolffelt, K. W., "Investigation of the Movement of Vortex Burst Position with Dynamically Changing Angle of Attack for a Schematic Delta Wing in a Water Tunnel with Correlation to Similar Studies in a Wind Tunnel," AGARD-CP-413, 1986.

[3]Soltani, M. R., Bragg, M. B., and Brandon, J. M., "Experimental Measurements on an Oscillating 70-Degree Delta Wing in Subsonic Flow," AIAA Paper 88-2576, June 1988.

[4]Torlund, P., "Wind Tunnel Force Measurements and Visualization on a 60-Degree Delta Wing in Oscillation, Stepwise Motion and Gusts," AGARD-CP-497, 1991.

[5]Fujii, K., and Schiff, L. B., "Numerical Simulation of Vortical Flows over a Strake-Delta Wing," *AIAA Journal*, Vol. 27, No. 9, 1989, pp. 1153–1162.

[6]Hartwich, P. M., and Hsu, C. M., "Numerical Study of the Vortex Burst Phenomenon for Delta Wings," AIAA Paper 88-0505, Jan. 1988.

[7]Ekaterinaris, J. A., Coutley, R. L., Schiff, L. B., and Platzer, M. F., "Numerical Investigation of the Flow over a Delta Wing at High Incidence," AIAA Paper 91-0753, Jan. 1991.

[8]Kandil, O. A., and Chuang, H. A., "Unsteady Navier–Stokes Computations past Oscillating Delta Wing at High Incidence," AIAA Paper 89-0081, Jan. 1989.

[9]Chaderjian, N. M., and Guruswamy, G. P., "Transonic Navier–Stokes Computations for an Oscillating Wing Using Zonal Grids," *Journal of Aircraft*, Vol. 29, No. 3, 1992, pp. 326–335.

[10]Ewald, B. F. R. (Ed.), "Wind Tunnel Wall Correction" AGARDograph 336, 1998.

[11]Thomas, J. P., and Lan, C. E., "The Simulation and Correction of Wind Tunnel Wall Interference on Delta Wing Lift Using Navier–Stokes and Euler Solutions," AIAA Paper 91-3300, Sept. 1991.

[12]Hsing, C. A., and Lan, C. E., "Low Speed Wind Tunnel Interference Assessment/Correction with Vortex Flow Effect," *Journal of Aircraft*, Vol. 34, No. 2, 1997, pp. 220–227.

[13]Bland, S. R., "The Two-Dimensional Oscillating Airfoil in a Wind Tunnel in Subsonic Flow," *SIAM Journal on Applied Mathematics*, Vol. 18, No. 4, 1970, pp. 830–848.

[14]Kuczka, D., "Hydridverfahren fur instationare Messungen in transsonischen Windkanalen am Beispiegel der harmonischen Nickschwingung," DFVLR-FB 88-19, Deutsche Forschungs und Versuchsanstalt fuer Luft und Raumfahrt, e. V., Cologne, Germany, 1988.

[15]Seebass, A. R., Fung, K. Y., and Przybytkowski, S. M., "Advances in the Understanding and Computation of Unsteady Transonic Flow," *Recent Advances in Aerodynamics*, Springer-Verlag, New York, 1986, pp. 3–37.

[16]Pulliam, T. H., "Euler and Thin Layer Navier Stokes Codes: ARC2D, ARC3D," Notes for the Computational Fluid Dynamics User's Workshop, Univ. of Tennessee Space Institute, Tullahoma, TN, March 1984.

[17]Hoffmann, K. A., *Computational Fluid Dynamics for Engineers*, Engineering Education System, Austin, TX, 1989.

[18]Pulliam, T. H., and Chaussee, D. S., "A Diagonal Form of an Implicit Approximate-Factorization Algorithm," *Journal of Computational Physics*, Vol. 39, No. 2, 1981, pp. 347–363.

[19]Thomas, P. D., and Lombard, C. K., "Geometric Conservation Law and Its Application to Flow Computations on Moving Grids," *AIAA Journal*, Vol. 17, No. 10, 1979, pp. 1030–1037.

[20]Brandon, J. M., and Shah, G. H., "Effect of Large Amplitude Pitching Motions on the Unsteady Aerodynamic Characteristics of Flat-Plate Wings," AIAA Paper 88-4331, Aug. 1988.

[21]Lee, Y. G. , "Navier–Stokes Analysis of Tunnel Wall Interference Effects on Pitching Delta Wings," Ph.D. Dissertation, Dept. of Aerospace Engineering, Univ. of Kansas, April 2001.